

Observed trends in auroral zone ion mode solitary wave structure characteristics using data from Polar

J. Dombeck, C. Cattell, and J. Crumley

School of Physics and Astronomy, University of Minnesota, Minneapolis, Minnesota

W. K. Peterson and H. L. Collin

Lockheed Martin, Palo Alto, California

C. Kletzing

Institute of Geophysics and Planetary Physics, University of Iowa, Iowa City, Iowa

Abstract. High-resolution ($8000 \text{ sample s}^{-1}$) data from the Polar Electric Field Instrument are analyzed for a study of ion mode solitary waves in upward current regions of the auroral zone. The primary focus of this study is the relations between velocity, maximum potential amplitude, and parallel structure width of these solitary waves (SWs). The observed SW velocities consistently lie, within error bars, between those of the H^+ and O^+ beams observed simultaneously by the Toroidal Imaging Mass-Angle Spectrograph (TIMAS) instrument. In addition, there is a trend that SW amplitudes are smaller when SW velocities are near the O^+ beam velocity and larger when SW velocities are near the H^+ beam velocity. These results are consistent with the observed ion mode SWs being a mechanism for the transfer of energy from the H^+ beam to the O^+ beam. A clear trend is also observed indicating larger amplitude with larger parallel spatial width. The results suggest that the observed solitary waves are a rarefactive ion mode associated with the ion two-stream instability.

1. Introduction

Solitary waves (SWs) were first observed in nature by the S3-3 satellite in the Earth's auroral zone [Temerin *et al.*, 1982]. These SWs were found to be moving at greater than $\sim 50 \text{ km s}^{-1}$. SWs have since been observed in many different regions of the magnetosphere [Matsumoto *et al.*, 1994; Bale *et al.*, 1998; Franz *et al.*, 1998; Cattell *et al.*, 1999] at measured speeds up to 5000 km s^{-1} [Ergun *et al.*, 1998]. Ion mode SWs travel with velocities which are of the order of the local sound speed or ion beam speeds (a few hundred km s^{-1} in the auroral zone). Electron mode SWs generally travel much faster (several thousand km s^{-1}) [Ergun *et al.*, 1998; Franz *et al.*, 1998; Cattell *et al.*, 1999]. Both ion and electron modes have been observed in the Earth's auroral zone [Mozer *et al.*, 1997; Ergun *et al.*, 1998; Bounds *et al.*, 1999].

The SWs detected by S3-3, at altitudes of $\sim 7000 \text{ km}$, were small in amplitude (typically $< 15 \text{ mV m}^{-1}$, $e\phi/kT < \sim 0.005$). Similar SWs were also observed in the auroral zone at roughly the same altitude by the Swedish Viking satellite [Boström *et al.*, 1988] and at lower altitude, $\sim 1700 \text{ km}$, by the Freja satellite [Dovner *et al.*, 1994]. A statistical survey [Mälkki *et al.*, 1993] using Viking data determined the dependence of ion mode SW observation on altitude, magnetic local time, and invariant latitude in the auroral zone. Viking also identified upward moving density depletions accompanying the SWs which were interpreted as the density perturbations of the SWs. The general properties of the observations from these satellites were compared with theory [Lotko and Kennel, 1983; Qian *et al.*, 1989] and with various simulations [Sato and Okuda, 1980; Barnes *et al.*, 1985; Marchenko and Hudson, 1995]. These comparisons seemed to indicate that the observed SWs were consistent with the general characteristics of ion acoustic SWs.

Recently, more capable satellites with higher data rates, simultaneous three-dimensional (3D) electric and magnetic field measurements and high-resolution particle detectors, notably Polar and FAST, have investigated the Earth's auroral zone leading to a wealth of data to be analyzed. Initial auroral zone results from Polar [Mozer *et al.*, 1997] include the discovery of much larger amplitude SWs ($\sim 200 \text{ mV m}^{-1}$) and timings of the ion mode SWs resulting in velocities of the order of the local sound speed, again consistent with an ion acoustic interpretation. This report concentrates on relations within individual “bursts” of data. Data from Polar during its southern hemisphere (perigee) passes through the auroral zone in 1997 at altitudes of $\sim 6000 - 7000 \text{ km}$ have been used. The focus of this study is the relations between maximum potential amplitude (Φ_{max}), velocity (v), and parallel structure width (δ).

The aim of this study is to compare the more recent Polar data to new simulations by Crumley *et al.* [2001] which model the plasma based on FAST observations. In addition, we will discuss our results in relation to previous observations, theoretical work, and simulations relating to ion acoustic SWs in the auroral zone. Lotko and Kennel [1983] expanded one-dimensional (1D) ion acoustic soliton theory into conditions more similar to the regions of the auroral zone where the ion mode SWs had been observed. Ion mode SWs have almost always been observed as negative potential structures propagating upward in the upward current regions of the auroral zone and in association with upward propagating ion beams. Lotko and Kennel included a cold beam ion population along with two electron and one ion background populations. The temperatures of all three of these background populations were much larger than that of the beam ions. Marchenko and Hudson [1995] performed two-dimensional (2D) electrostatic particle simulations involving three populations, a cold background ion population, a drifting electron population, and an ion beam population, with $T_e/T_i=20$. The formation of negative potential SWs propagating downward relative to the beam of the order of the local sound speed (c_s) was common in both the Marchenko and Hudson simulations as well as the theoretical development of Lotko and Kennel. Such SWs would appear to propagate upward in the satellite frame at $\sim 1 c_s$ less than the beam speed.

The effects of the presence of a $\text{H}^+ \text{-O}^+$ two-stream instability in the auroral zone as related to ion acoustic waves and SWs were investigated theoretically by Bergmann *et al.* [1988] and Qian *et al.* [1989]. As a result, several additional regions of possible existence for ion acoustic SWs were determined. Mälkki *et al.* [1989] provide a theoretical review of the various theories which attempt to explain ion mode SWs in the auroral zone.

The remainder of this report is organized as follows: section 2 describes the method used for the current study; section 3 includes the study results; section 4 contains discussion about the current study; and section 5 then gives a general conclusion of the study's key points.

2. Methodology

The data for this study are from the Polar satellite, during high-resolution ($125 \mu\text{s}$ sample rate), 6 s “bursts” of electric field measurements obtained by the Polar Electric Field Instrument (EFI) [Harvey *et al.*, 1995] in the auroral zone at altitudes of $\sim 1 R_E$. Within each burst, SWs are automatically identified (criteria described below), and their characteristics are determined. Data from several other instruments onboard

Polar are also used for the study. The background magnetic field is determined from Polar fluxgate magnetometer data [Russell *et al.*, 1995]. Ion composition data is provided by the Toroidal Imaging Mass-Angle Spectrograph (TIMAS) [Shelley *et al.*, 1995], and Hydra provides high time resolution electron and ion distribution measurements [Scudder *et al.*, 1995].

Solitary waves are isolated structures characterized by a bipolar electric field pulse in the direction of the background magnetic field. The SWs of interest here move past the satellite in a very short time (~ 0.01 s) and are moving much faster than the satellite (several hundred km s^{-1} compared to a few km s^{-1}). To determine the physical structure of the SW, its velocity must first be determined. This is done using an interferometer. Assuming the SW is propagating parallel to the background magnetic field (**B**), the velocity can be determined when Polar has one of its spin plane boom pairs nearly aligned with **B**. Figure 1 depicts this situation with a SW moving toward the satellite (in this case antiparallel to **B**). In the example pictured, the 3-4 boom pair is nearly aligned with **B**. (Only the spin plane probes are shown in Figure 1). A summary of the velocity calculation procedure is also included. As Polar cartwheels in its orbit, its spin plane stays nearly aligned with **B** allowing general usage of the described procedure.

To determine velocities, the ability of the EFI on Polar to independently measure the voltage of each probe relative to the spacecraft is used. First the angles of the spin plane booms relative to **B** are determined, and the designation of the mostly parallel (3-4 in Figure 1) and mostly perpendicular (1-2) pairs is made. While, in principle, all six probe voltages are measured simultaneously, this is not strictly true. Polar takes electric field measurements by sampling even numbered probes first and then odd numbered probes 25 μs later. To correct for this “stagger,” the arrays of voltage measurements for each probe are first splined to a common time base of 25 μs . A “center” voltage, V_C , array is calculated by taking the mean of the two spin plane probe voltages mostly perpendicular to **B**. V_C is taken to be the potential of the plasma at the center of the spacecraft relative to the actual spacecraft potential had the spacecraft not been there. The perpendicular probes are used in this manner rather than the actual spacecraft potential because the probes and the spacecraft body respond differently to changes in plasma density. Use of V_C rather than the spacecraft potential provides a more accurate measurement of the electric field. The interferometer potential differences, V_+ and V_- , between the probe in the +**B** direction and V_C and between V_C and the probe in the -**B** direction, respectively, are then calculated. The cross correlations for the time series V_+ and V_- are then computed shifting the data, one time step at a time, relative to each other. The time shift corresponding to the highest cross correlation is considered to be the time delay for the SW to propagate from the probe in the +**B** direction to the spacecraft center. Dividing the effective boom length along **B** of this probe by the determined time delay yields the SW’s velocity. This procedure results in positive velocities and time delays corresponding to Earthward moving SWs in the region of interest for this study (i.e., Southern Hemisphere where the magnetic field is upward).

The time shifted cross correlations are also used to determine error in the measured time delay and thus the error in the determined velocities. Figure 2 shows a typical cross correlation versus time delay relation. The error in time delay is defined as the first point to either side of the peak cross correlation value (c_{max}) for which $1-c > 1.2 (1-c_{\text{max}})$. This

Figure 1

Figure 2

range is indicated by the vertical lines in Figure 2. The error range is typically 4-5 points (100-125 μ s) in either direction. Since the velocity is inversely proportional to the time delay, this results in more accurate velocity determinations for lower velocities. It also results in asymmetric error bars, larger in the direction corresponding to higher velocity.

This analysis is only possible when one pair of spin plane probes are nearly aligned with **B**. In addition, interference related to magnetic shadowing is also possible when the probe pair is too nearly aligned with **B**. Analysis has given us confidence in the results of the described procedure for probe angles of 4° - 25° to **B**. This probe alignment constraint gives the described technique $\sim 50\%$ temporal coverage in any burst.

Figure 3 depicts a sample output of the analysis for a SW within an EFI burst recorded on June 16, 1997, at ~ 1525 UT. Figure 3a depicts V_+ and V_- , dotted and dashed, respectively. As can be seen V_+ lags V_- , indicating an upward propagating SW. For comparison, the heavy black line in Figure 3a shows the negative of E_z (the component of the electric field parallel to the background magnetic field) multiplied by the effective boom length (L_B). E_z is computed from all six of the EFI probes. The time delay analysis resulted in a maximum cross correlation of 0.9888 at a time delay of 200 μ s, which results in a SW velocity (v) of ~ 300 km s^{-1} with an error range of ~ 225 -500 km s^{-1} . The parallel structure width (δ) and potential amplitude at time t (Φ_t) are then determined by

$$\delta = v \tau \quad (1)$$

$$\Phi_t = -v \sum_{t'=0}^t E_z \Delta t' , \quad (2)$$

where τ is the temporal width and $\Delta t'$ is the sampling time step. The total temporal extent of the SW, τ , marked by the vertical bars in Figure 3, is defined as the points where the outside slopes of the SW E_z change sign. To compare widths in this study with other studies which utilize the half widths of best fit gaussians, divide widths in this report by roughly a factor of 4. This width method was chosen, in particular, because our study allows for a variety of SW shapes, not just those closely resembling the derivative of a Gaussian. It also facilitates simple calculation of other parameters and selection criteria as described below. The pictured example has $\tau = 9.775$ ms, resulting in $\delta \sim 3.0$ km. Figure 3b shows the potential (Φ_t). The maximum potential amplitude (Φ_{\max}) is then defined as the potential difference between the SW extremum (within the vertical bars) and the mean of all non-SW points (outside the vertical bars), in this case ~ 43 volts. Since the velocity is a linear factor to both δ and Φ_{\max} and the velocity error bars are substantial, the errors in δ and Φ_{\max} are dominated by those in velocity. Using key parameter data from Hydra, δ and Φ_{\max} can be normalized by λ_D and e/kT_e , respectively. This is done primarily for reference only, but it also allows comparison of relations between different bursts. This normalization is quite rough with the plasma being decidedly non-Maxwellian and the error in the normalization factors being of the order of $\pm 25\%$ owing to the low resolution of the key parameter data.

Since SWs have been observed with various shapes, from Gaussian-type potentials as in Figure 3 to extremely flat-topped potentials, it was our desire to include as many types of SWs in our analysis as possible, not limiting selection by shape. Therefore the selection criteria are more complex, but we believe more robust, than simply searching for shapes that appear as derivatives of a Gaussian. SWs are identified within the E_z data array for each burst. While a complete

Figure 3

description of this process is beyond the scope of this report, the general procedure follows (the numerical limits pertaining to the study in this report are listed). First all extrema are found. An extremum is defined as a local maximum or minimum, monotonic for at least two actual data points in either direction. Each maximum is compared with nearby minima to determine if the pair represents the maximum and minimum of a SW. First the time extent is determined as defined above, then an analysis region is defined (0.25τ before the first vertical bar to 0.25τ after the second vertical bar). The analysis region so defined generally contains of the order of 500 data points. If this entire analysis region does not meet the satellite angle requirements described above, the SW is rejected. If any additional peak is found between the chosen extrema which is greater than 0.4 times the selected extrema, the SW is rejected. If any data point greater than 0.5 times the selected extrema is found in the analysis region outside of the chosen extrema, the SW is rejected. If the maximum cross correlation is less than 0.88, the SW is rejected. Finally, to assure that the SW is not significantly affected by other waves, if the DC offset between V_+ and V_- is greater than the peak to peak amplitude of the SW, the SW is rejected. For each SW meeting these criteria, v , δ , and Φ_{\max} are determined and normalized based on the Hydra electron moments.

3. Results

Figure 4c is a typical potential amplitude versus velocity plot for the SWs in one burst of the current study. The parallel and one component of the perpendicular electric field for the burst are shown in Figures 4b and 4a, respectively. The dashed (dotted) vertical bar in Figure 4c marks the approximate H^+ (O^+) beam velocity (relative to the spacecraft). Each point represents one SW identified within the burst using the procedure describe in section 2. The beam velocities were determined from the location of the peaks in the H^+ and O^+ distribution functions produced by the TIMAS instrument onboard Polar. Plate 1 shows the TIMAS ion distribution functions for the time of this burst. Figure 4 shows that the SW velocities are generally spread between the H^+ and O^+ beam velocities with a trend of increasing potential amplitude with greater SW speed (relative to the spacecraft). These results are common in all three of the bursts which were compared with TIMAS data. Not uncommonly, a few SW speeds are measured faster than the H^+ beam speed. In almost all of these cases, the velocity error bar extends below the H^+ beam speed. In addition, it must be remembered that the beam speeds indicated are extremely rough. Taking these factors into account, we are rather confident in the claim that the observed SWs in this study have velocities between the H^+ and O^+ beam velocities. This is also consistent with the velocity results of the *Crumley et al.* [2001] simulations as well as with several of the previous theories [*Mäkkä et al.*, 1989].

No clear relation was found during initial attempts to compare the SW velocities to the sound speed. In particular, the expectation, based on ion acoustic theory for a H^+ - O^+ plasma [*Qian et al.*, 1989], that SW velocities would be supersonic at $\sim 1 c_s$ slower than the beam velocity were not observed. In the case of Figure 4, the sound speeds are $c_{S-H^+} \sim 200 \text{ km s}^{-1}$ and $c_{S-O^+} \sim 40 \text{ km s}^{-1}$. Clearly, no supersonic SWs slower than the O^+ beam are present. Additionally, a cutoff at $\sim 1 c_s$ slower than the H^+ beam velocity is not apparent but also not ruled out.

Figure 4

Plate 1

When discussing the correlation between Φ_{\max} and velocity, it must be noted that Φ_{\max} is the relative potential maximum along the trajectory of the satellite and not the maximum amplitude of the entire 3D structure. Preliminary analysis has indicated that often a large perpendicular component of the electric field, up to the order of the parallel electric field, is associated with the observed SWs. This indicates that the SWs are likely 3D structures, as opposed to planar, possibly with perpendicular widths comparable to the parallel widths. This is consistent with the scale size results of the recent simulations by *Crumley et al.* [2001]. (Note that the 3D shape of electron solitary waves has been discussed by *Ergun et al.* [1998] and *Franz et al.* [2000]; however, a detailed study of the 3D structure of ion SWs has not yet been made. Such a study is underway.) Therefore the actual structure potential maximum will vary relative to that observed, depending on which portion of the 3D structure the satellite trajectory traverses. Even so, the overall trend of increasing amplitude with increasing speed is quite clear in our results, as is the lack of an obvious direct relation between SW velocity and sound speed.

Another comparison of interest is Φ_{\max} versus physical structure width (δ). This comparison can compensate, to some degree, for the centering of the trajectory, and both parameters can also easily be normalized for comparison between bursts. Figure 5 is a summary plot of Φ_{\max} versus δ (normalized by e/kT_e and λ_D , respectively) for three different bursts studied. Error bars are omitted for clarity. There is a well-defined trend of increasing amplitude with increasing spatial width for each burst. While intuitively this makes sense, larger structures in amplitude being larger spatially as well, it is in contrast to small amplitude 1D ion acoustic soliton theory which predicts the opposite relation ($\delta \sim \Phi_{\max}^{-1/2}$). This, in combination with the observed velocities, indicates that current small amplitude 1D ion acoustic soliton theory does not describe the observed ion mode SWs. A complete theory of large amplitude ion acoustic SWs may have different characteristics, however, as suggested by *Berthomier et al.* [1998]. Unfortunately such a theory has not yet been completed.

Figure 5

4. Discussion

In the upward current regions of the auroral zone, there is a potential gradient which accelerates ionospheric ions into the observed H^+ and O^+ beams. The mass difference between the ions results in the observed velocity difference of the beams. However, this velocity difference results in a two-stream instability which attempts to shift energy from the H^+ beam to the O^+ beam, in the satellite frame. It is our assertion that this instability results in the observed ion mode SWs and that these SWs are a key mechanism for the described energy exchange. Theory has shown that, in an H^+ - O^+ two-stream interaction, ion acoustic waves can grow to observable size [*Bergmann et al.*, 1988] and that the interaction can produce solitary waves at velocities similar to those observed [*Qian et al.*, 1989]. Therefore these SWs may be ion acoustic in nature. Recent simulations, which include both H^+ and O^+ beams [*Crumley et al.*, 2001] produce SWs moving at velocities relative to the beam velocities which are in agreement with those observed. In addition to the inclusion of the second ion species, these recent simulations removed the cold background ion and electron populations since such populations are generally not present in the region of interest [*Strangeway et al.*, 1998; *McFadden et al.*, 1999]. These newer simulations also indicate that the vast majority of ion

heating occurs during the period when the SWs are present. Additionally, the H^+ and O^+ beam velocities move closer together (energy is exchanged) dramatically during this same period.

The described energy exchange may also account for the observed Φ_{\max} versus velocity relation. If the SWs are a mechanism to transfer energy from the H^+ beam to the O^+ beam, the closer the SW velocity is to the O^+ beam velocity, the less energy can be transferred to the O^+ beam. This may account for the observed larger Φ_{\max} values nearer the H^+ beam velocity. Although not observed in the current study, there may also be an evolution of SW velocity. A reasonable example of such evolution would be rapid growth due to instability near the H^+ beam velocity, then gradual dissipation as the SW velocity approaches the O^+ beam velocity.

5. Conclusion

We have made the first study of ion solitary waves to compare SW velocities to simultaneously observed ion beam speeds and to examine the relationship of the maximum potential to structure size and velocity. This study has shown the following: (1) SW velocities are consistently, within error bars, between the associated H^+ and O^+ beam velocities. (2) There is no clear relation between SW velocity and the sound speed. (3) The Φ_{\max} increases with increasing SW velocity, relative to the spacecraft. Larger Φ_{\max} occurs nearer the H^+ beam velocity, and smaller Φ_{\max} occurs nearer the O^+ beam velocity. (4) The Φ_{\max} increases with increasing spatial width (δ).

These results are in good agreement with recent simulations by *Crumley et al.* [2001], which had plasma populations consisting of hot electrons and, O^+ and H^+ beams. The results (particularly 2, 3, and 4) are not consistent with small amplitude 1D ion acoustic soliton theory. These inconsistencies may not exist in large amplitude theory.

These observations suggest that the ion mode SWs in the auroral zone are the result of the nonlinear development of an ion two stream instability. This condition may not be required to produce ion mode SWs, since the simulations by *Crumley et al.* [2001] also indicate that SWs can form with just one (H^+) ion beam.

Acknowledgments. The authors thank the NASA Polar spacecraft and operations teams and the instrument engineering and software teams at UCB, University of Iowa, and Lockheed Martin. The authors also thank C. T. Russell for allowing use of the DC magnetic field data and Jack Scudder for allowing use of plasma measurements from the instruments for which they are Principle Investigators. This research was supported by NASA NAG5-3182, NAG5-7885, NAG5-3217, NAG5-3302, NGT5-50251, NGT5-50293, and NAS5-30302.

Janet G. Luhman thanks the referees for their assistance in evaluating this paper.

References

- Bale, S. D., P. J. Kellogg, D. E. Larson, R. P. Lin, K. Goetz, and R. P. Lepping, Bipolar electrostatic structures in the shock transition region: Evidence of electron phase space holes, *Geophys. Res. Lett.*, **25**, 2929, 1998.
- Barnes, C., M. K. Hudson, and W. Lotko, Weak double layers in ion acoustic turbulence, *Phys. Fluids*, **28**, 1055, 1985.
- Bergmann, R., I. Roth, and M. K. Hudson, Linear stability of the H^+ - O^+ two-stream interaction in a magnetized plasma, *J. Geophys. Res.*, **93**, 4005, 1988.
- Berthomier, M., R. Pottelette, and M. Malingre, Solitary waves and weak double layers in a two-electron temperature auroral plasma, *J. Geophys. Res.*, **103**, 4261, 1998.
- Boström, R., G. Gustafsson, B. Holback, G. Holmgren, H. Koskinen, and P. Kintner, Characteristics of solitary waves and weak double

- layers in the magnetospheric plasma, *Phys. Rev. Lett.*, **61**, 82, 1988.
- Bounds, S. R., R. F. Pfaff, S. F. Knowlton, F. S. Mozer, M. A. Temerin, and C. A. Kletzing, Solitary potential structures associated with ion and electron beams near 1 R_E altitudes, *J. Geophys. Res.*, **104**, 28,709, 1999.
- Cattell, C. A., J. Dombeck, J. R. Wygant, F. S. Mozer, and C. A. Kletzing, Comparisons of Polar satellite observations of solitary wave velocities in the plasma sheet boundary and high altitude cusp to those in the auroral zone, *Geophys. Res. Lett.*, **26**, 425, 1999.
- Crumley, J. P., C. A. Cattell, R. L. Lysak, and J. P. Dombeck, Studies of ion solitary waves using simulations including hydrogen and oxygen beams, *J. Geophys. Res.*, in press, 2001.
- Donver, P. O., A. I. Eriksson, R. Boström, and B. Holback, Freja multiprobe observations of electrostatic solitary structures, *Geophys. Res. Lett.*, **21**, 1827, 1994.
- Ergun, R. E., C. W. Carlson, J. P. McFadden, F. S. Mozer, G. T. Delory, W. Peria, C. C. Chaston, M. Temerin, I. Roth, L. Muschietti, R. Elphic, R. Strangeway, R. Pfaff, C. A. Cattell, D. Klumppar, E. Shelley, W. Peterson, E. Moebius, and L. Kistler, FAST satellite observations of large-amplitude solitary structures, *Geophys. Res. Lett.*, **25**, 2041, 1998.
- Franz, J. R., P. M. Kintner, and J. S. Pickett, Polar observations of coherent electric field structures, *Geophys. Res. Lett.*, **25**, 1277, 1998.
- Franz, J. R., P. M. Kintner, C. E. Seyler, J. S. Pickett, and J. D. Scudder, On the perpendicular scale of electron phase-space holes, *Geophys. Res. Lett.*, **27**, 169, 2000.
- Harvey, P., F. S. Mozer, D. Pankow, J. Wygant, N. C. Maynard, H. Singer, W. Sullivan, P. B. Anderson, R. Pfaff, T. Aggson, A. Pedersen, C.-G. Fälthammar, and P. Tanskannen, The Electric Field Instrument on the Polar Satellite, in *The Global Geospace Mission*, edited by C. T. Russell, p. 583, Kluwer Acad., Norwell, Mass., 1995.
- Lotko, W., and C. Kennel, Spiky ion acoustic waves in collisionless auroral plasma, *J. Geophys. Res.*, **88**, 381, 1983.
- Mälkki, A., H. Koskinen, R. Boström, and B. Holback, On theories attempting to explain observations of solitary waves and weak double layers in the magnetosphere, *Phys. Scr.*, **39**, 787, 1989.
- Mälkki, A., A. I. Eriksson, P.-O. Donver, R. Boström, B. Holback, G. Holmgren, and H. E. J. Koskinen, A statistical survey of auroral solitary waves and weak double layers. 1. Occurrence and net voltage, *J. Geophys. Res.*, **98**, 15,521, 1993.
- Marchenko, V., and M. Hudson, Beam-driven ion acoustic solitary waves in the auroral acceleration region, *J. Geophys. Res.*, **100**, 19,791, 1995.
- Matsumoto, H., H. Kojima, T. Miyatake, Y. Omura, M. Okada, I. Nagano, and M. Tsutui, Electrostatic solitary waves (ESW) in the magnetotail: BEN wave forms observed by GEOTAIL, *Geophys. Res. Lett.*, **21**, 2915, 1994.
- McFadden, J. P., C. W. Carlson, and R. E. Ergun, Microstructure of the auroral acceleration region as observed by FAST, *J. Geophys. Res.*, **104**, 14,453, 1999.
- Mozer, F. S., R. Ergun, M. Temerin, C. Cattell, J. Dombeck, and J. Wygant, New features in time domain electric field structures in the auroral acceleration region, *Phys. Rev. Lett.*, **79**, 1281, 1997.
- Qian, S., W. Lotko, and M. K. Hudson, Oxygen acoustic solitary waves in a magnetized plasma, *J. Geophys. Res.*, **94**, 1339, 1989.
- Russell, C. T., R. C. Snare, J. D. Means, D. Pierce, D. Dearborn, M. Larson, G. Barr, and G. Le, The GGS/Polar Magnetic Fields Investigation, in *The Global Geospace Mission*, edited by C. T. Russell, p. 563, Kluwer Acad., Norwell, Mass., 1995.
- Sato, T., and H. Okuda, Ion-acoustic double layers, *Phys. Rev. Lett.*, **44**, 740, 1980.
- Scudder, J., et al., Hydra- A 3-D electron and ion hot plasma instrument for the Polar spacecraft of the GGS mission, in *The Global Geospace Mission*, edited by C. T. Russell, p. 459, Kluwer Acad., Norwell, Mass., 1995.

- Shelley, J., et al., The Toriodal Imaging Mass-Angle Spectrograph (TIMAS) for the Polar Mission, in *The Global Geospace Mission*, edited by C. T. Russell, p. 497, Kluwer Acad., Norwell, Mass., 1995.
- Strangeway, R. J., L. Kepko, R. C. Elphic, C. W. Carlson, R. E. Ergun, J. P. McFadden, W. J. Peria, G. T. Delory, C. C. Chaston, M. Temerin, C. A. Cattell, E. Mobius, L. M. Kistler, D. M. Klumpar, W. K. Peterson, E. G. Shelley, and R. F. Pfaff, FAST observations of VLF waves in the auroral zone: evidence of very low plasma densities, *Geophys. Res. Lett.*, 25, 2065, 1998.
- Temerin, M., K. Cerney, W. Lotko, and F. S. Mozer, Observations of double layers and solitary waves in the auroral plasma, *Phys. Rev. Lett.*, 48, 1175, 1982.

C. Cattell, J. Crumley, and J. Dombeck, School of Physics and Astronomy, University of Minnesota, 116 Church Street, S.E., Minneapolis, MN 55455. (cattell@fields.space.umn.edu; crumley@fields.space.umn.edu; johnd@fields.space.umn.edu)

H. L. Collin and W. K. Peterson, Lockheed Martin ATC, L9-42, B255, 3251 Hanover Street, Palo Alto, CA 94304. (collin@aspen.spasci.com; pete@willow.colorado.edu)

C. Kletzing, Institute of Geophysics and Planetary Physics, University of Iowa, Rm 203 Van Allen Hall, Iowa City, Iowa, 52242. (craig-kletzing@uiowa.edu)

(Received September 15, 2000; revised December 13, 2000; accepted December 14, 2000.)

Copyright 2001 by the American Geophysical Union

Paper number 2000JA000355
0148-0227/01/2000JA000355\$12.00

Figure Captions:

Figure 1. A schematic drawing illustrating how the propagation velocity is determined. The four spin plane electric field probes of the Polar spacecraft are shown. In this case, probes 3 and 4 are nearly aligned with the geomagnetic field, \mathbf{B} , down which a SW is propagating. The mean of the perpendicular probe voltages, probes 1 and 2, is used as a central reference voltage to remove effects due to the difference in response of the spacecraft body and the probes to local plasma density.

Figure 1. A schematic drawing illustrating how the propagation velocity is determined. The four spin plane electric field probes of the Polar spacecraft are shown. In this case, probes 3 and 4 are nearly aligned with the geomagnetic field, \mathbf{B} , down which a SW is propagating. The mean of the perpendicular probe voltages, probes 1 and 2, is used as a central reference voltage to remove effects due to the difference in response of the spacecraft body and the probes to local plasma density.

Figure 2. A typical cross correlation versus time delay plot. The determined time delay error which translates into the velocity error is represented by the vertical bars.

Figure 2. A typical cross correlation versus time delay plot. The determined time delay error which translates into the velocity error is represented by the vertical bars.

Figure 3. Sample SW velocity calculation output. The calculated velocity (with error range), delay between V_+ and V_- , and the cross correlation at this delay are listed at the top. (a) V_+ (V_-), dotted (dashed), as described in Figure 1. The heavy black line in Figure 3a is the negative of the field-aligned electric field multiplied by the effective boom length. (b) The integration of the parallel electric field from left to right using the calculated velocity as described in the text. The vertical bars represent the determined extents of the SW width. The time width so determined is listed to the upper right of Figure 3a. The calculated spatial parallel width and maximum potential are listed to the lower left. These values are derived from the structure velocity as described in the text.

Figure 3. Sample SW velocity calculation output. The calculated velocity (with error range), delay between V_+ and V_- , and the cross correlation at this delay are listed at the top. (a) V_+ (V_-), dotted (dashed), as described in Figure 1. The heavy black line in Figure 3a is the negative of the field-aligned electric field multiplied by the effective boom length. (b) The integration of the parallel electric field from left to right using the calculated velocity as described in the text. The vertical bars represent the determined extents of the SW width. The time width so determined is listed to the upper right of Figure 3a. The calculated spatial parallel width and maximum potential are listed to the lower left. These values are derived from the structure velocity as described in the text.

Figure 4. Potential amplitude versus velocity plot, Figure 4c for the SWs identified in the EFI burst taken at ~0057 UT, April 1, 1997. The left scale lists the absolute potential amplitude, while the right scale is normalized by the electron temperature. The dashed and dotted vertical bars represents the rough H^+ and O^+ beam velocities as determined from the locations of the peaks of the TIMAS distribution data in Figure 5. The grouping of SW velocities between the two beam speeds is apparent in this figure. Figures 4b and 4a show the parallel and one perpendicular component of the electric field, respectively, for the entire burst.

Figure 4. Potential amplitude versus velocity plot, Figure 4c for the SWs identified in the EFI burst taken at ~0057 UT, April 1, 1997. The left scale lists the absolute potential amplitude, while the right scale is normalized by the electron temperature. The dashed and dotted vertical bars represents the rough H^+ and O^+ beam velocities as determined from the locations of the peaks of the TIMAS distribution data in Figure 5. The grouping of SW velocities between the two beam speeds is apparent in this figure. Figures 4b and 4a show the parallel and one perpendicular component of the electric field, respectively, for the entire burst.

Plate 1. The TIMAS distribution plot for the time of the EFI burst in which the SWs of Figure 4 were detected. (a) The H^+ and (b) O^+ velocity distributions are shown, respectively. In Plates 1a and 1b the direction of the background magnetic field, \mathbf{B} , is to the right.

Figure 5. Normalized solitary potential amplitude versus parallel spatial width for three studied EFI bursts. A trend of increasing amplitude with increasing width is apparent within each burst. Also indicative in this plot is the general observed spatial width of $\sim 10\text{--}15 \lambda_D$ and potential amplitude of $\sim 0.03\text{--}0.07 T_e$ for the solitary waves in this study. Note widths are ~ 4 times larger than Gaussian half widths used in other studies.

[illegible]

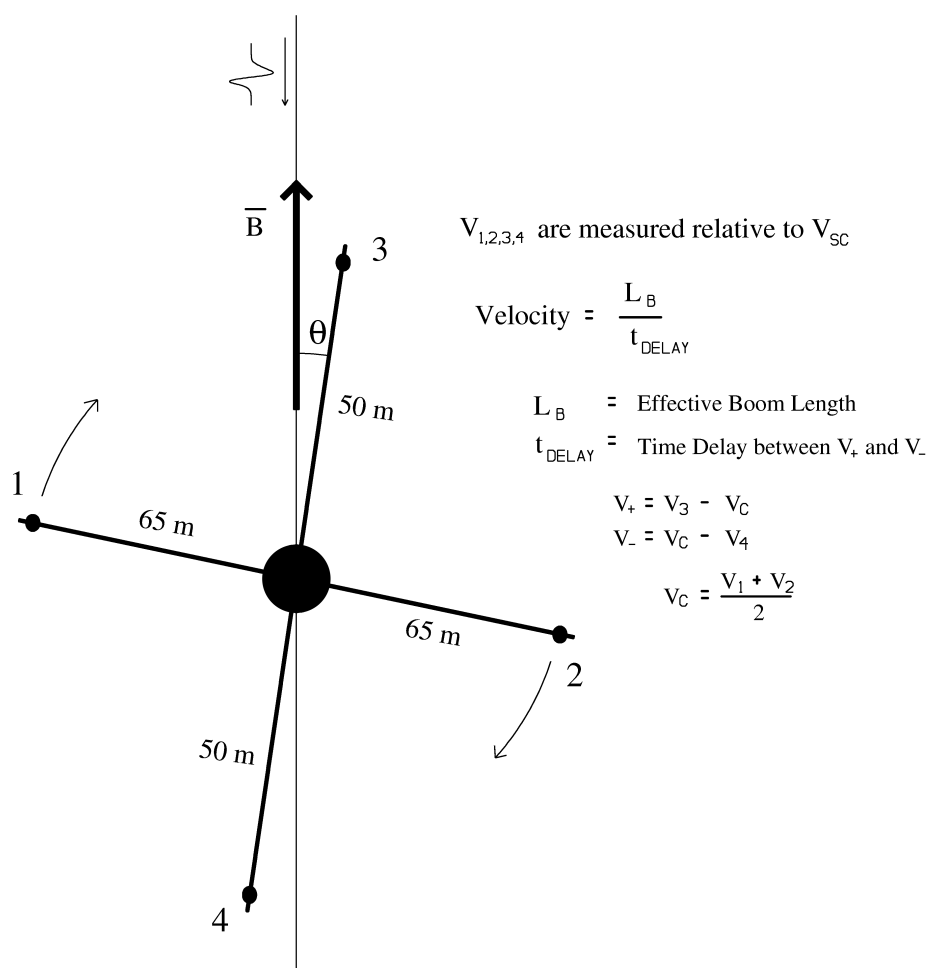


Figure 1.

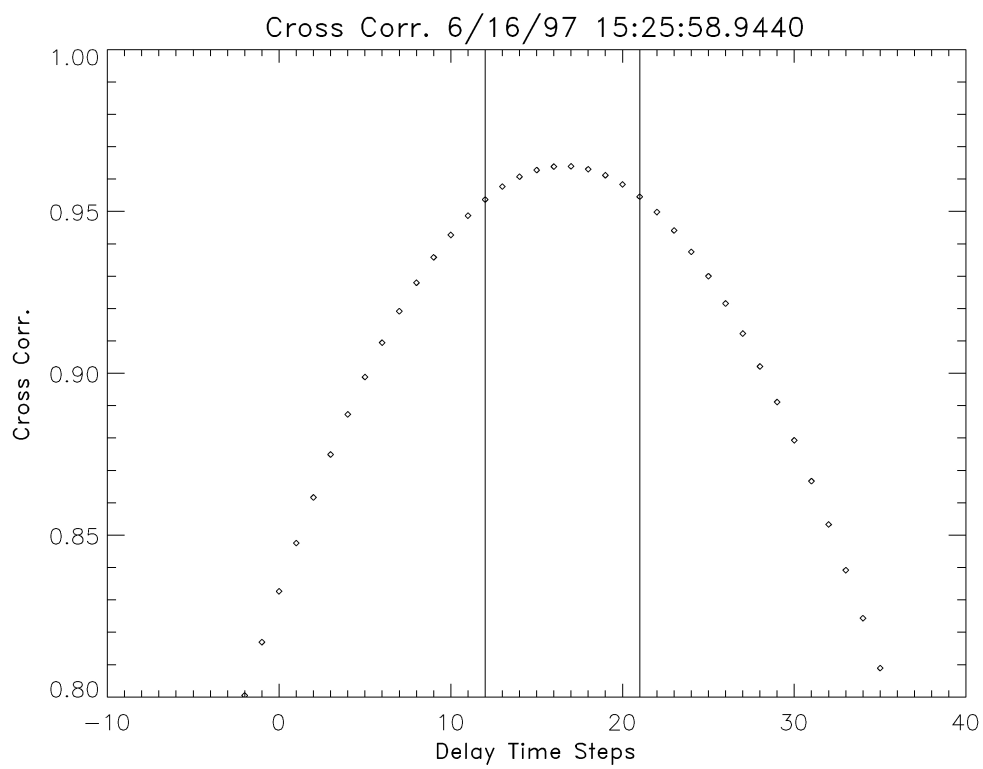


Figure 2.

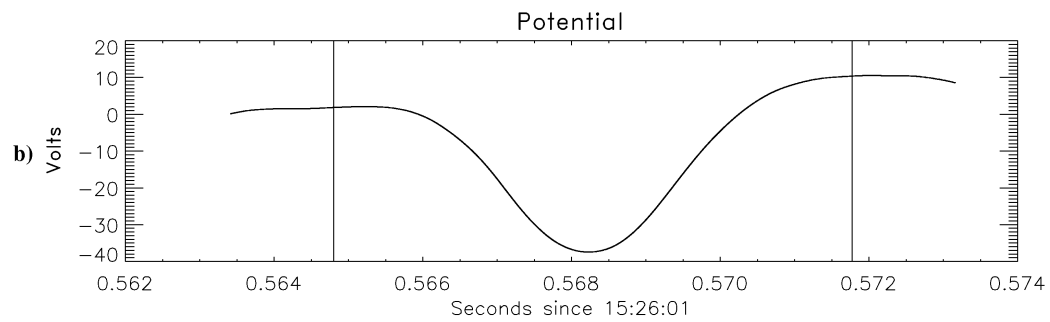
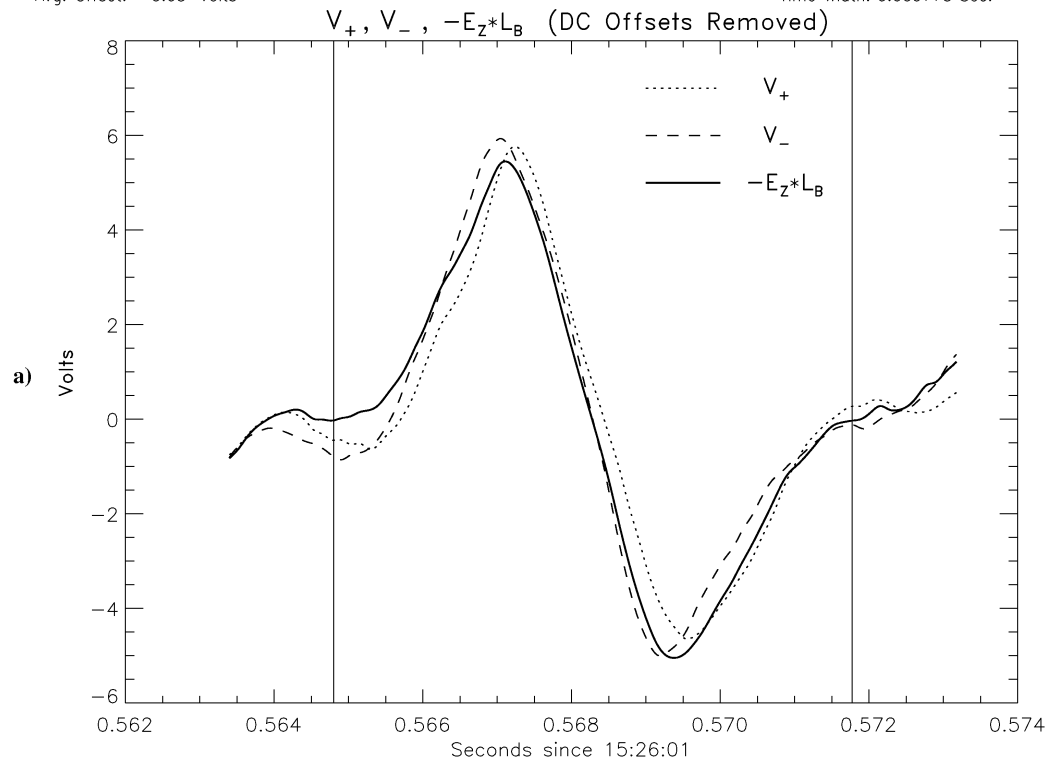
Nearest Boom to +DC B-Field = 1

FILE 1 = /cdrom/dt.6.16.97.B_V1U

VELOCITY (km/s)	DELAY (Seconds)	CROSS-CORRELATION @ DELAY	EFFECTIVE BOOM LENGTH (L_B)
-311	-0.0002000	0.9888	@ AVG. TOTAL ANGLE = 62.27 m
SPLINED			
Range -498 - -226			

Avg. Offset: 0.03 Volts

Time Width: 0.009775 Sec.



Structure Width: 3.0400 Km	Range (Km): 2.2091 - 4.8679
Potential: -43.1963 Volts	Range (Volts): -27.3333 - -76.8393

Figure 3.

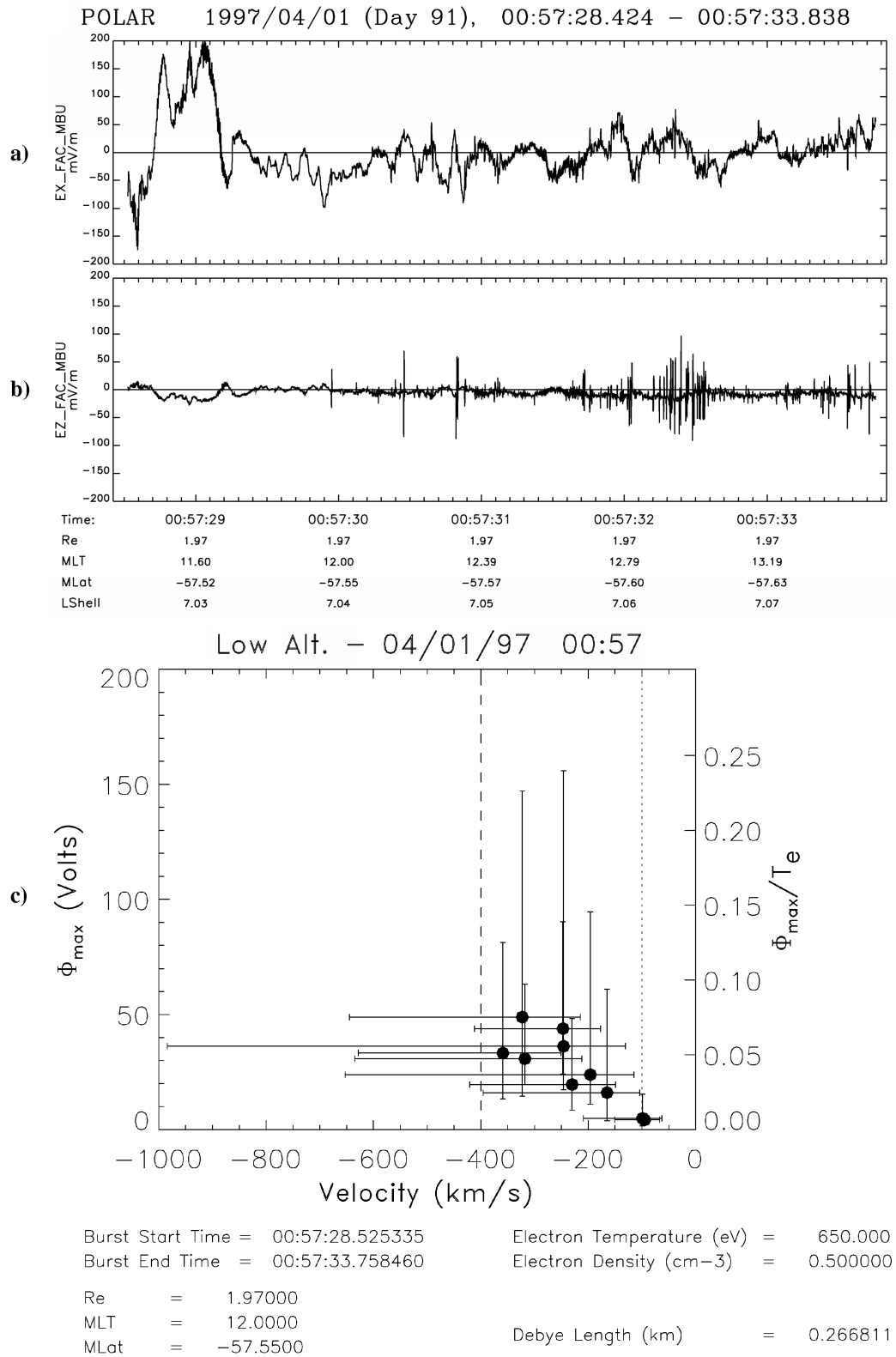


Figure 4.

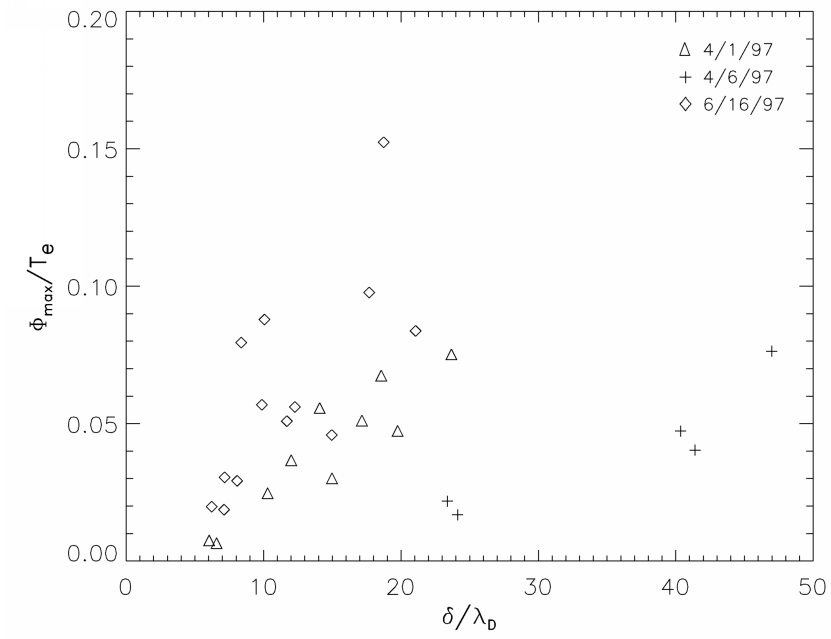
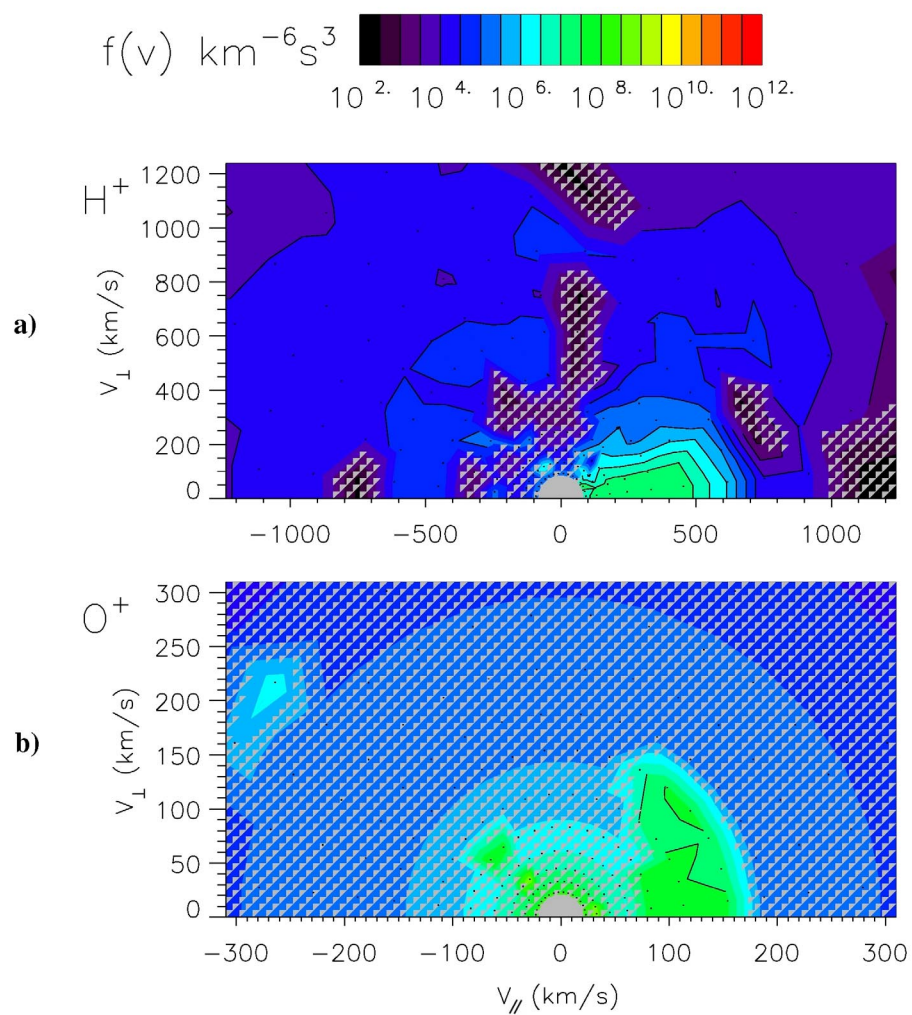


Figure 5.

**Plate 1.**